

# Retrieval of phytoplankton and colored detrital matter absorption coefficients with remote sensing reflectance in an ultraviolet band

Jianwei Wei\* and Zhongping Lee

School for the Environment, University of Massachusetts Boston, 100 Morrissey Blvd., Boston, Massachusetts 02125, USA

\*Corresponding author: Jianwei.Wei@umb.edu

Received 23 October 2014; revised 6 December 2014; accepted 6 December 2014;  
posted 9 December 2014 (Doc. ID 225562); published 22 January 2015

The light absorption of phytoplankton and colored detrital matter (CDM), which includes contribution of gelbstoff and detrital matters, has distinctive yet overlapping features in the ultraviolet (UV) and visible domain. The CDM absorption ( $a_{dg}$ ) increases exponentially with decreasing wavelength while the absorption coefficient of phytoplankton ( $a_{ph}$ ) generally decreases toward the shorter bands for the range of 350–450 nm. It has long been envisioned that including ocean color measurements in the UV range may help the separation of these two components from the remotely sensed ocean color spectrum. An attempt is made in this study to provide an analytical assessment of this expectation. We started with the development of an absorption decomposition model [quasi-analytical algorithm (QAA)-UV], analogous to the QAA, that partitions the total absorption coefficient using information at bands 380 and 440 nm. Compared to the retrieval results relying on the absorption information at 410 and 440 nm of the original QAA, our analyses indicate that QAA-UV can improve the retrieval of  $a_{ph}$  and  $a_{dg}$ , although the improvement in accuracy is not significant for values at 440 nm. The performance of the UV-based algorithm is further evaluated with *in situ* measurements. The limited improvement observed with the field measurements highlights that the separation of  $a_{dg}$  and  $a_{ph}$  is highly dependent on the accuracy of the ocean color measurements and the estimated total absorption coefficient. © 2015 Optical Society of America

*OCIS codes:* (010.4450) Oceanic optics; (010.0280) Remote sensing and sensors; (010.1030) Absorption; (010.0010) Atmospheric and oceanic optics; (010.4455) Oceanic propagation; (280.4991) Passive remote sensing.

<http://dx.doi.org/10.1364/AO.54.000636>

## 1. Introduction

Phytoplankton and colored detrital matters (CDM), including the gelbstoff/CDOM and detritus, are two important participants in the biogeochemical cycles of global oceans (see Table 1 for notations and abbreviations). As the primary producer, the phytoplankton absorbs solar radiation and sequesters the atmospheric carbon during photosynthesis. It is estimated that about 100 petagrams of carbon (half of the total fixed carbon on earth) are fixed by the

phytoplankton each year in the upper ocean [1]. CDM is an optically active component regulating the light penetration, particularly at blue and ultraviolet (UV) bands, and profoundly impacts the photochemistry process [2]. In addition, CDM represents a great pool of the dissolved organic carbon [3]. Accurate description of the spatial and temporal changes of phytoplankton and CDM in the oceans allows for a better understanding of the roles of ocean in the global carbon cycles [4].

Decades of studies have proved that remote sensing of ocean color can provide quantitative information on the phytoplankton and CDM dynamics in the global oceans [5]. There are generally two categories

Table 1. Symbols, Notations, and Abbreviations

Symbols	Definitions	Units
$A$	Total absorption coefficient	$m^{-1}$
$a_{ph}$	Absorption coefficient due to phytoplankton	$m^{-1}$
$a_{dg}$	Absorption coefficient due to gelbstoff and detritus	$m^{-1}$
$a_g$	Absorption coefficient due to gelbstoff	$m^{-1}$
$a_w$	Absorption coefficient due to pure seawater	$m^{-1}$
$b_{bp}$	Backscattering coefficient due to particles	$m^{-1}$
$b_{bw}$	Backscattering coefficient due to pure seawater	$\mu Wcm^{-2} sr^{-1} nm^{-1}$
$L_{wn}$	Normalized water-leaving radiance	$sr^{-1}$
$R_{rs}$	Remote sensing reflectance just above water surface	$sr^{-1}$
$r_{rs}$	Remote sensing reflectance just below water surface	$nm^{-1}$
$S$	Slope of absorption spectrum $a_{dg}(\lambda)$	dimensionless
$\zeta$	Spectral ratio of phytoplankton absorption	dimensionless
$\xi$	Spectral ratio of CDM absorption	
CDM	Colored detrital matter	
CDOM	Colored dissolved organic matter	
IOCCG	International Ocean Color Coordinating Group	
MAPE	Mean absolute percentage error	
PACE	Pre-Aerosol, Clouds, and Ocean Ecosystem	
QAA	Quasi-analytical algorithm	
RMSE	Root mean square error	
SeaWiFS	SeaWiFS Bio-optical Archive and Storage System	
UV	Ultraviolet	

of inversion algorithms employed for the derivation of the two components from ocean color, i.e., the semi-analytical and the empirical algorithms. The semi-analytical algorithms differ among themselves with distinctive theoretical bases and mathematical schemes [6–8]. For instance, the QAA of Lee *et al.* [6] partitions the total absorption spectrum into the phytoplankton absorption ( $a_{ph}$ ) and the CDM absorption ( $a_{dg}$ ) according to the absorption ratios at two blue bands (410 and 440 nm). These absorption products have been increasingly used for the parameterization of the biogeochemical status of the oceans [9–12]. Empirical ocean color algorithms operate on the relationships empirically built between the remote sensing reflectance band ratios and the desired biological/chemical parameters, which include the chlorophyll a concentration (CHL,  $mg\ m^{-3}$ ). The operational algorithm for deriving CHL in near-surface oceanic water is a polynomial function constructed from *in situ* database [13]. This type of algorithm usually does not simultaneously separate the CDM optical properties from those of phytoplankton.

The current and heritage satellite ocean color sensors image the oceans in predetermined visible to shortwave infrared bands, with bands in the visible usually centered at wavelengths around 410, 440, 490, 550, and 670 nm. The 410 nm band is designed because the disparity between the phytoplankton absorption and the CDM absorption at this band is large and therefore offers potential to separate the two absorption coefficients [14–16]. Interestingly, empirical ocean color algorithms rarely use the 410 nm band for such a separation [17,18].

The available measurements of ocean color in the UV domain are very limited, and the inclusion of the UV ocean color observation for the retrieval of water

constituents is scarce. One of the few datasets was collected by the Global Imager (GLI), which measured the ocean color including a UV band at 380 nm. Based on the GLI measurements, Mitchell and Kahru [19] reported that the absorption of the gelbstoff at 300 nm can be well retrieved from the ratio of the normalized water-leaving radiance ( $L_{wn}$ ) at 380 and 545 nm for the California coastal waters. The analyses of *in situ* measured ocean color in the south Pacific Gyre further confirmed the favorable role of UV ocean color for assessment of CDOM absorption at UV bands [20]. Other studies were devoted to the estimation of the gelbstoff absorption at the UV bands from the empirical algorithms composed of only band ratios in the visible domain [21,22].

Both phytoplankton and CDOM/CDM absorb light in the same spectral domain [23] (Fig. 1). The overlapping spectral signature limits the accuracy in the simultaneous separation of these two components from the ocean color observations [11,24]. This is particularly true with the empirically derived chlorophyll a concentration from the band ratio algorithms, for which large errors and uncertainties exist due to the interference of the CDM component [25–29].

The next generation of satellite ocean color sensors, Pre-Aerosol, Clouds, and Ocean Ecosystem (PACE), is being planned to provide an extension of past observations and synergy with its precursor missions for inland, coastal, and oceanic waters [30]. PACE will include measurements in the UV-A bands (e.g., 340 to 380 nm). Generally accurate determination of water-leaving radiance in the UV domain from a satellite sensor is challenging because of its relatively weak contributions to the total

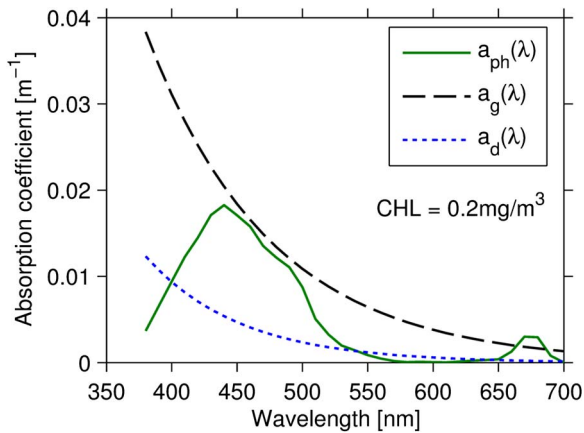


Fig. 1. Example of spectral absorption coefficient with chlorophyll a concentration 0.2 mg/m<sup>3</sup>. The difference in the magnitudes of  $a_{ph}$  and  $a_{dg}$  spectra reaches the maxima at the shortest wavelengths.

top-of-atmosphere radiance. A recent study, however, indicated that the UV water-leaving radiance can be derived accurately with a more advanced atmospheric correction scheme [31]. Then it is important and necessary to know whether the separation of phytoplankton and CDM absorption coefficient will be improved with ocean color information in the UV domain.

The objective of this study is henceforth to answer, through an analytical evaluation, to what extent the ocean color measurements in the UV band will help the retrieval of CDM and phytoplankton absorption coefficients. This study starts with refining the QAA by involving a UV band (termed as QAA-UV hereafter) in a procedure analogous to and comparable with the original QAA scheme of Lee *et al.* [6]. The difference is that the QAA-UV model decomposes the total absorption spectrum utilizing the absorption coefficients at 380 and 440 nm, while the “standard” QAA model uses 410 and 440 nm bands. This stepwise analytical method allows for diagnosis and identification of the source of uncertainties in the analytically derived absorption coefficients of both phytoplankton and CDM.

## 2. Refined Absorption Decomposition Algorithm

### A. Synthetic UV Dataset

A dataset consisting of 500 spectra of the inherent optical properties (IOPs) from UV to visible bands (380–700 nm) is created based on the International Ocean-Color Coordinating Group (IOCCG) dataset [32]. The original IOCCG dataset has a spectral range as 400–800 nm (with a wavelength increment of 10 nm). The synthetic dataset extends the IOCCG data to a UV band at 380 nm. The selection of 380 nm as the shortest UV wavelength is based on the fact that such a band was proposed for the ocean color satellite sensors [33,34] and was once tested by the GLI ocean color satellite [19]. And, likely there are still adequate water-leaving radiance signals at this

band in oceanic waters for reliable estimation from a satellite ocean color sensor [31].

The dataset adopts a four-component model [35,36] for the creation of the absorption spectra. The total absorption coefficient ( $a$ , unit: m<sup>-1</sup>) is parameterized as

$$a(\lambda) = a_w(\lambda) + a_{ph}(\lambda) + a_d(\lambda) + a_g(\lambda), \quad (1)$$

with the four contributing components being pure seawater ( $a_w$ , m<sup>-1</sup>), phytoplankton ( $a_{ph}$ , m<sup>-1</sup>), detritus ( $a_d$ , m<sup>-1</sup>), and gelbstoff ( $a_g$ , m<sup>-1</sup>). The absorption of  $a_w$  from 380–700 nm is from Pope and Fry [37]. To extend the  $a_{ph}$  spectra to 380 nm, a linear spectral relationship between the wavelength and  $a_{ph}$  for each phytoplankton absorption spectrum was developed based on the  $a_{ph}$  data at bands of 400, 410, 420, 430, and 440 nm, and  $a_{ph}(380)$  is then calculated from this relationship. Although such a linearity assumption for the extrapolation of  $a_{ph}(\lambda)$  to 380 nm may not exactly represent the variability of  $a_{ph}$  spectrum in this wavelength range occurring in nature, it is sufficient for our investigation here ( $R^2$  is generally >0.95; data not presented), as the focus is on the impact of including a UV band on the decomposition of the total absorption coefficient.

The  $a_d$  and  $a_g$  spectra in the IOCCG synthetic dataset increase exponentially with the decrease of wavelength [e.g., 23]; it is thus straightforward to extend these two spectra to 380 nm.

The total backscattering coefficient ( $b_b$ , m<sup>-1</sup>) dataset is composed of three contributors including the scattering of pure seawater ( $b_{bw}$ , m<sup>-1</sup>), phytoplankton ( $b_{bph}$ , m<sup>-1</sup>), and detritus ( $b_{bd}$ , unit: m<sup>-1</sup>):

$$b_b(\lambda) = b_{bw}(\lambda) + b_{bph}(\lambda) + b_{bd}(\lambda). \quad (2)$$

The backscattering coefficient of pure seawater is from Morel [38]. The particulate backscattering coefficient due to phytoplankton and detritus follows a power-law function of wavelength (Gordon and Morel, 1983); thus it is also straightforward to extend the two spectra to 380 nm.

The remote sensing reflectance right below the water surface ( $r_{rs}$ , sr<sup>-1</sup>) is simulated from the synthesized  $a(\lambda)$  and  $b_b(\lambda)$  based on a model developed by Lee *et al.* [39], which accounted for the different effects of molecular and particle scatterings [39]:

$$r_{rs} = g_w \frac{b_{bw}}{a + b_b} + g_p \frac{b_{bp}}{a + b_b}, \quad (3)$$

where the parameter  $g_w$  is equal to 0.113 sr<sup>-1</sup> for nadir radiance; the model parameter  $g_p$ (sr<sup>-1</sup>) is modeled as below [39]:

$$g_p = G_0 \left[ 1 - G_1 \exp \left( -G_2 \frac{b_{bp}}{a + b_b} \right) \right], \quad (4)$$

where the model parameters  $G_0$ ,  $G_1$ , and  $G_2$  are determined as 0.197 sr<sup>-1</sup>, 0.636, and 2.552,

respectively, for a nadir-viewing sensor. The remote sensing reflectance just above the sea surface ( $R_{rs}$ , sr<sup>-1</sup>) is then derived from the following model [40,41]:

$$R_{rs} = \frac{T \cdot r_{rs}}{1 - r \cdot Q \cdot r_{rs}}. \quad (5)$$

In Eq. (5), the model parameters  $T \approx 0.52$  and  $\gamma Q \approx 1.7$  for the optically deep waters and a nadir-viewing sensor [6].

From the above, a synthetic dataset including 500 sets of  $R_{rs}$ ,  $a$ , and  $b_b$  spectra in the spectral range of 380–700 nm (10 nm step) is obtained. Ranges of main parameters for the synthetic data are summarized in Table 2.

### B. Decomposition of Total Absorption Coefficient

There are many semi-analytical algorithms available for the estimation and decomposition of the total absorption coefficient from the remote sensing reflectance [e.g., 6,7,35]. Here we follow the stepwise procedure of QAA developed by Lee *et al.* [6], mainly because of its clearness in the derivation processes and lack of residual error between the input  $R_{rs}$  and the output  $R_{rs}$ . QAA divides the analytical inversion process into two consecutive sections: Section 1 derives the total absorption coefficient from the  $R_{rs}$  spectrum and Section 2 further decomposes the derived total absorption coefficient into components of  $a_{ph}$  and  $a_{dg}$  ( $a_{dg} = a_d + a_g$ ). For the refined model that utilizes a UV band (henceforth, QAA-UV), it takes exactly the same steps as the original QAA for the derivation of the total absorption and back-scattering coefficients. The scheme to decompose the total absorption coefficient, i.e., Section 2 of the “standard” QAA, is the focus of this study and is detailed as below. For easy comparison, the detailed

formulation of QAA-UV is presented in Table 3, along with the original QAA partition algorithm.

Briefly, both QAA-UV and QAA utilize a combination of analytical inversion and a few empirical relationships for separating  $a_{ph}$  and  $a_{dg}$  from the total absorption spectrum (Table 3). A system of two linear equations for the total absorption coefficient at two wavelengths is established [6], which consists of the spectral ratios of  $a_{ph}$  and  $a_{dg}$ , respectively,

$$\zeta = \frac{a_{ph}(\lambda_1)}{a_{ph}(\lambda_2)}, \quad (6)$$

$$\xi = \frac{a_{dg}(\lambda_1)}{a_{dg}(\lambda_2)}. \quad (7)$$

When the partition factors  $\zeta$  and  $\xi$  are known,  $a_{dg}$  at  $\lambda_2$  can be readily derived from the known total absorption spectrum [6]:

$$a_{dg}(\lambda_2) = \frac{[a(\lambda_1) - a_w(\lambda_1)] - \zeta[a(\lambda_2) - a_w(\lambda_2)]}{\xi - \zeta}. \quad (8)$$

The key difference between QAA-UV and QAA is the spectral band ( $\lambda_1$ ) used for the decomposition. The “standard” QAA utilizes a wavelength pair at 410 nm ( $\lambda_1$ ) and 440 nm ( $\lambda_2$ ), while the proposed QAA-UV utilizes a wavelength pair at 380 nm ( $\lambda_1$ ) and 440 nm ( $\lambda_2$ ).

Similar to Lee *et al.* [6], empirical relationships were developed for the estimation of  $\zeta$  and  $\xi$  in QAA-UV, with the empirical coefficients determined by an optimization procedure. In QAA, both  $\zeta$  and  $\xi$  are parameterized as functions of  $r_{rs}(440)/r_{rs}(550)$ . In QAA-UV, however, the estimation of  $\zeta$  is modified to use  $r_{rs}(380)/r_{rs}(550)$  as the input (see step 1 in Table 3), while the estimation of  $\xi$  is modified to use  $r_{rs}(380)/r_{rs}(440)$  as the input (see 2 in Table 3).

When  $a_{dg}(440)$  is determined from Eq. (8), the absorption coefficient of CDM can be extended to the full spectrum following the exponential decay function [23]:

$$a_{dg}(\lambda) = a_{dg}(440) \cdot e^{-S(\lambda-440)}. \quad (9)$$

Then the spectral absorption  $a_{ph}(\lambda)$  will be determined by subtracting  $a_{dg}(\lambda)$  and  $a_w(\lambda)$  from  $a(\lambda)$ :

Table 2. Ranges of Main Parameters for the Synthetic Data and Field Data

No.	Parameter	Synthetic Data	Field Data
1	$a_{ph}(410)/a_{ph}(440)$	0.604–1.003	0.426–1.046
2	$a_{ph}(380)/a_{ph}(440)$	0.060–0.958	0.221–1.290
3	$a_{dg}(410)/a_{dg}(440)$	1.314–1.807	1.177–2.405
4	$a_{dg}(380)/a_{dg}(440)$	1.739–3.273	1.482–4.266
5	$S$	0.009–0.020	0.007–0.047
6	$R_{rs}(380)/R_{rs}(440)$	0.334–1.276	0.304–2.289
7	$R_{rs}(440)/R_{rs}(550)$	0.123–6.773	0.207–4.994

Table 3. Absorption Decomposition Algorithms Used by QAA-UV and QAA Models

Step No.	QAA-UV	QAA <sup>a</sup>
1	$\zeta = \frac{a_{ph}(380)}{a_{ph}(440)} = p_1 + \frac{p_2}{p_3 + r_{rs}(380)/r_{rs}(550)}$ $p_1 = 0.4596, p_2 = 2.874 \times 10^{-6}, p_3 = -0.0626$	$\zeta = \frac{a_{ph}(410)}{a_{ph}(440)} = p_1 + \frac{p_2}{p_3 + r_{rs}(440)/r_{rs}(550)}$ $p_1 = 0.74, p_2 = 0.06, p_3 = 0.8$
2	$\xi = \frac{a_{dg}(380)}{a_{dg}(440)} = e^{-S(380-440)} S = p_1 + \frac{p_2}{p_3 + r_{rs}(380)/r_{rs}(440)}$ $p_1 = 0.00854, p_2 = 0.005055, p_3 = 0.2236$	$\xi = \frac{a_{dg}(410)}{a_{dg}(440)} = e^{-S(410-440)} S = p_1 + \frac{p_2}{p_3 + r_{rs}(440)/r_{rs}(550)}$ $p_1 = 0.015, p_2 = 0.002, p_3 = 0.6$

<sup>a</sup>Source: [http://www.ioccg.org/groups/Software\\_OCA/QAA\\_v5.pdf](http://www.ioccg.org/groups/Software_OCA/QAA_v5.pdf)

$$a_{ph}(\lambda) = a(\lambda) - a_{dg}(\lambda) - a_w(\lambda). \quad (10)$$

### C. Model Evaluations

The performance of the absorption decomposition algorithm is evaluated by comparing the retrieved products with the known simulated values. The root mean square error (RMSE) is a simple estimator for the model accuracy and represents the standard deviation of the differences between the predictions and observations and is often adopted as a measure of predictive power for the ocean color inversion models [32]. The unbiased RMSE error is computed in log space as

$$\text{RMSE} = \left[ \frac{1}{n} \sum_{i=1}^n (\log_{10} X_i^{\text{est}} - \log_{10} X_i)^2 \right]^{1/2}, \quad (11)$$

where  $X_i^{\text{est}}$  and  $X_i$  refer to the algorithm-retrieved  $i^{\text{th}}$  value and the  $i^{\text{th}}$  true value, respectively, and  $n$  is the total number of valid observations. The normalized root mean square error (nRMSE) is then determined by normalizing RMSE to the absolute value of the mean of observations  $X_i$ . The coefficient of determination  $R^2$  of the Type II regression is also derived, in log space.

The synthetic dataset spans a fairly wide dynamic range, with the chlorophyll a concentration in a range of  $0.03 \text{ mg m}^{-3}$  to  $30 \text{ mg m}^{-3}$  and 45% of the dataset with CHL less than  $0.7 \text{ mg m}^{-3}$ , which corresponds to the majority of oceanic waters. With the synthesized total absorption coefficient and remote sensing reflectance, the QAA-UV and QAA partition algorithms (in Table 3) are first employed to derive  $a_{ph}(440)$  and  $a_{dg}(440)$ . Scatter plots of the decomposed absorption coefficients and the known values are presented in Fig. 2. For the model estimated  $a_{ph}(440)$ , the error metrics RMSE and  $R^2$  are not much different between the two sets of model estimations, while the model-data bias is much suppressed by QAA-UV [Figs. 2(a) and 2(b)]. For the model-derived  $a_{dg}(440)$ , both the RMSE and the biases are greatly reduced by QAA-UV [Figs. 2(c) and 2(d)]. It is apparent that the QAA-UV algorithm provides better estimation for both  $a_{ph}(440)$  and  $a_{dg}(440)$  for such cases.

The error statistics of model derivations in all wavelengths is given in Table 4. The RMSE (and nRMSE) and bias for the estimated spectral  $a_{dg}$  monotonically decrease with decreasing wavelengths and reach a minimum at the UV band. This feature is due to the exponential decay of the CDM absorption coefficient and echoes the higher accuracy of  $a_{dg}(\lambda)$

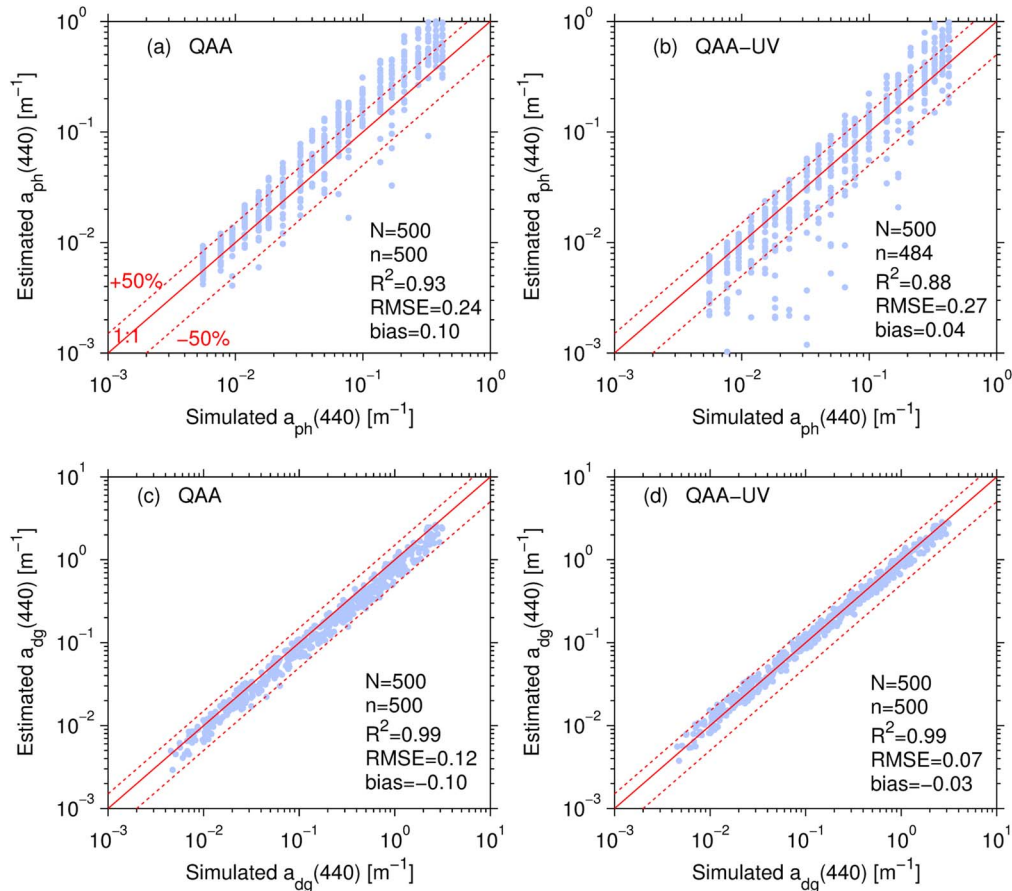


Fig. 2. Scatterplots of the model-derived and the known absorption coefficients. The solid line denotes the relation 1:1; the dashed lines refer to  $\pm 50\%$  errors.  $N$  is the total number of observations, while  $n$  is the total number of valid observations.

Table 4. Error Statistics between the Model-Estimated Absorption Coefficient and the Simulated Absorption<sup>a</sup>

	Band (nm)	<i>N</i>	<i>n</i>	<i>R</i> <sup>2</sup>	RMSE (m <sup>-1</sup> )	nRMSE (%)	Bias (m <sup>-1</sup> )
<i>a<sub>ph</sub></i> (λ)	380	500(500)	492(499)	0.83(0.92)	<b>0.30(0.36)</b>	<b>18.7(21.9)</b>	<b>0.03(0.08)</b>
	410	500(500)	471(500)	0.87(0.93)	<b>0.27(0.27)</b>	<b>20.5(20.0)</b>	<b>0.03(0.10)</b>
	440	500(500)	484(500)	0.88(0.93)	0.27(0.24)	21.4(19.1)	<b>0.04(0.10)</b>
	490	500(500)	474(500)	0.83(0.90)	0.33(0.29)	22.5(19.8)	<b>0.03(0.07)</b>
	550	500(500)	396(482)	0.80(0.84)	<b>0.41(0.47)</b>	<b>22.2(23.5)</b>	<b>0.03(0.05)</b>
<i>a<sub>dg</sub></i> (λ)	380	500(500)	500(500)	1.0(1.0)	<b>0.02(0.04)</b>	<b>5.2(9.3)</b>	<b>-0.02(-0.08)</b>
	410	500(500)	500(500)	1.0(1.0)	<b>0.05(0.08)</b>	<b>7.2(12.6)</b>	<b>-0.03(-0.10)</b>
	440	500(500)	500(500)	0.99(0.99)	<b>0.07(0.12)</b>	<b>8.8(15.0)</b>	<b>-0.03(-0.10)</b>
	490	500(500)	500(500)	0.98(0.97)	<b>0.12(0.20)</b>	<b>10.2(17.6)</b>	<b>-0.03(-0.07)</b>
	550	500(500)	500(500)	0.96(0.93)	<b>0.17(0.29)</b>	<b>11.1(19.6)</b>	<b>-0.02(-0.05)</b>

<sup>a</sup>The QAA derivations are presented within parentheses. *N* is the total number of observations, and *n* is the number of valid observations. The bold values indicate that the accuracy of model estimations has been improved by the QAA-UV algorithm.

often obtained at shorter wavebands where the magnitudes of *a<sub>dg</sub>* are larger [22]. Slightly different than estimated *a<sub>dg</sub>*, the RMSE error and the bias of the *a<sub>ph</sub>* estimations exhibit differential wavelength dependence. And the relatively small RMSE and bias are found at the band of 440 nm, where the phytoplankton absorption spectrum often peaks.

Based on this comparison, the QAA-UV algorithm generates more accurate estimates for *a<sub>dg</sub>*(λ), with overall smaller RMSE and nRMSE errors and biases than estimated *a<sub>ph</sub>*(λ) (Table 4). It is noted that the bias in the estimated *a<sub>ph</sub>* is opposite that of the estimated *a<sub>dg</sub>* in Table 4 since two component absorption coefficients are related through Eq. (10) and the *a*(λ) is error free for the synthetic data.

### 3. Error Budgets

#### A. Source of Errors

Errors or uncertainties in the algorithm-derived *a<sub>ph</sub>* and *a<sub>dg</sub>* in the QAA system originate from the modeled partition factors as well as the algorithm steps including the estimated total absorption coefficient at the reference wavelength (550 nm) and the model input (the remote sensing reflectance).

Accurate modeling of the two partition factors, ζ(λ<sub>1</sub>, λ<sub>2</sub>) and ξ(λ<sub>1</sub>, λ<sub>2</sub>), is important in obtaining accurate retrievals of *a<sub>ph</sub>*(λ) and *a<sub>dg</sub>*(λ) from the total absorption spectra through the QAA system [see Eq. (8)]. Over the entire range of the synthetic data, the modeling error for ζ(380, 440) is actually a few times larger than that of ζ(410, 440) (ε = 31% versus ε = 9%). In contrast, the errors of modeled ξ(380, 440) are smaller than the modeled ξ(410, 440) (ε = 12.6% versus ε = 23%). To further probe into the impacts of these errors on the accuracy of retrieved *a<sub>ph</sub>* and *a<sub>dg</sub>*, a sensitivity analysis was performed. First, the true values of ζ(λ<sub>1</sub>, λ<sub>2</sub>) and empirically modeled values of ξ(λ<sub>1</sub>, λ<sub>2</sub>) (step 2 in Table 3) are used to decompose the true total absorption coefficient into *a<sub>ph</sub>* and *a<sub>dg</sub>*. Then, we replace the ζ(λ<sub>1</sub>, λ<sub>2</sub>) and ξ(λ<sub>1</sub>, λ<sub>2</sub>) with their empirically determined values and true values, respectively, and repeat the procedure of absorption coefficient

decomposition. The RMSE errors and bias of the estimated component absorption coefficients by QAA-UV are illustrated in Fig. 3. As would be expected, the algorithm-derived *a<sub>ph</sub>* and *a<sub>dg</sub>* are subject to greater errors when the partition factor ξ(λ<sub>1</sub>, λ<sub>2</sub>) is not accurately determined. It is apparent the QAA system is much more sensitive to ξ than ζ in the visible bands. At the band of 380 nm, the differential contribution of modeled ξ and ζ parameters to the errors in the absorption estimation becomes minimal [Figs. 3(a) and 3(c)].

The next immediate question is on the influence of erroneous estimation of *a*(λ) on the model decomposition results. To answer this question, the absorption coefficient *a*(λ) is first estimated using the algorithms of the latest QAA model of Lee *et al.* [42]. The QAA-UV partition algorithm is then implemented to decompose the estimated *a*(λ) spectra. Therefore the observed errors in the derived *a<sub>ph</sub>*(λ) and *a<sub>dg</sub>*(λ) are solely due to the errors from the estimated *a*(λ) as well as the modeled ζ(λ<sub>1</sub>, λ<sub>2</sub>) and ξ(λ<sub>1</sub>, λ<sub>2</sub>). Another parallel decomposition experiment was also performed with the true absorption coefficient, for which the errors are only associated with the modeled ζ(λ<sub>1</sub>, λ<sub>2</sub>) and ξ(λ<sub>1</sub>, λ<sub>2</sub>). As indicated in Fig. 4, both the RMSE error and bias in the separated *a<sub>ph</sub>*(λ) and *a<sub>dg</sub>*(λ) can be significantly higher due to the erroneous estimation of *a*(λ).

#### B. Model Uncertainty

Because the QAA-UV partition algorithm has followed the same stepwise procedure as the original QAA, the uncertainty in *a<sub>ph</sub>*(440) and *a<sub>dg</sub>*(440) can be evaluated analytically following the error propagation strategy demonstrated by Lee *et al.* [43],

$$\begin{aligned}
 [\Delta a_{dg}(\lambda_2)]^2 = & \frac{(\Delta a_{12\zeta})^2}{(\xi - \zeta)^2} + \left[ \frac{a_{12\zeta} - a_w(\lambda_1) + \zeta a_w(\lambda_2)}{(\xi - \zeta)^2} \Delta \xi \right]^2 \\
 & + \left[ \frac{a_w(\lambda_2) - a(\lambda_2)}{\xi - \zeta} \Delta \zeta \right. \\
 & \left. + \frac{a_{12\zeta} - a_w(\lambda_1) + \zeta a_w(\lambda_2)}{(\xi - \zeta)^2} \Delta \zeta \right]^2, \quad (12)
 \end{aligned}$$

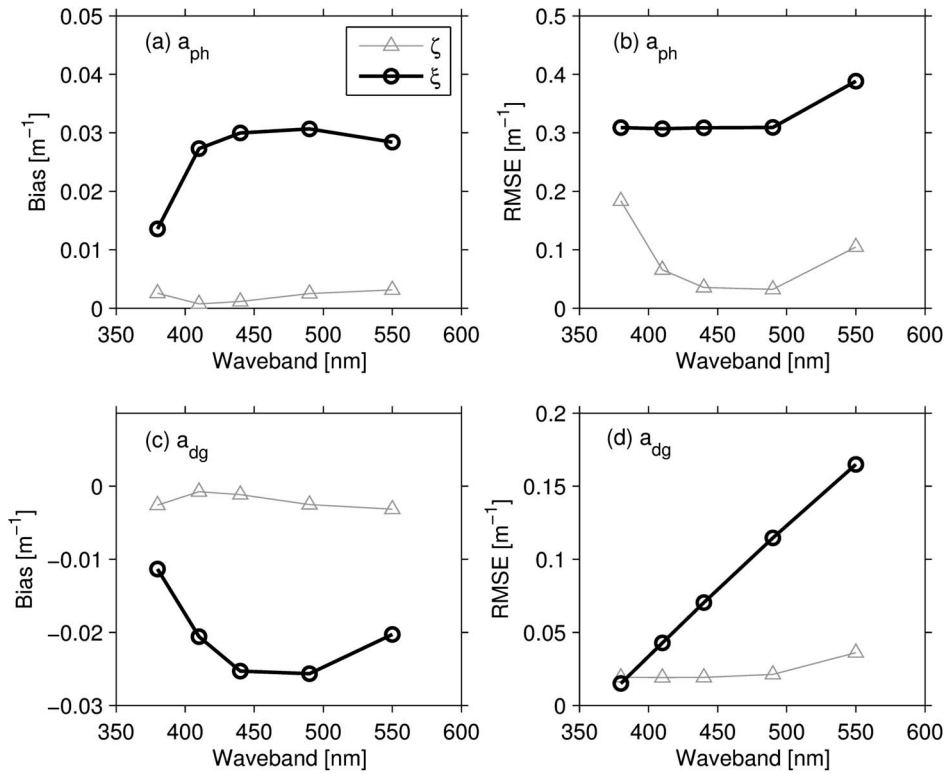


Fig. 3. Sensitivity of model retrievals to the partition factors. The symbol “ $\Delta$ ” denotes the errors induced by modeled  $\xi$ ; the symbol “ $\circ$ ” is the error caused by modeled  $\zeta$ .

$$\begin{aligned}
 [\Delta a_{ph}(\lambda_2)]^2 &= \frac{(\Delta a_{21\xi})^2}{(\xi - \zeta)^2} + \left[ \frac{a_{21\xi} + a_w(\lambda_1) - \xi a_w(\lambda_2)}{(\xi - \zeta)^2} \Delta \zeta \right]^2 \\
 &+ \left[ \frac{a(\lambda_2) - a_w(\lambda_2)}{\xi - \zeta} \Delta \xi \right]^2 \\
 &+ \frac{a_{21\xi} + a_w(\lambda_1) - \xi a_w(\lambda_2)}{(\xi - \zeta)^2} \Delta \xi \right]^2. \quad (13)
 \end{aligned}$$

In the above equations,  $a_{12\zeta} = a(\lambda_1) - \zeta a(\lambda_2)$  and  $a_{21\xi} = \xi a(\lambda_2) - a(\lambda_1)$ . The wavelength  $\lambda_2$  is fixed to 440 nm;  $\lambda_1$  refers to 380 nm for the QAA-UV algorithm and 410 nm for the QAA algorithm.

Based on the CDM exponential decay model [Eq. (9)], the spectral uncertainty  $a_{dg}(\lambda)$  can be derived from the uncertainty propagation scheme as below:

$$[\Delta a_{dg}(\lambda)]^2 = \left[ \frac{\partial a_{dg}(\lambda)}{\partial a_{dg}(440)} \Delta a_{dg}(440) \right]^2 + \left[ \frac{\partial a_{dg}(\lambda)}{\partial S} \Delta S \right]^2. \quad (14)$$

The partial derivatives (also known as the sensitivity coefficients) in this equation can be readily derived from Eq. (9). Although it is reported that  $a_{dg}(440)$  and  $S$  are correlative in some places [e.g., 44], the empirical relationship is not globally stable. For illustration, the spectral uncertainty of phytoplankton absorption  $\Delta a_{ph}$  can be represented as the following from Eq. (1):

$$[\Delta a_{ph}(\lambda)]^2 = [\Delta a(\lambda)]^2 + [\Delta a_{dg}(\lambda)]^2 + 2 \cdot \sigma_{xy}. \quad (15)$$

Note that the uncertainties  $\Delta a(\lambda)$  and  $\Delta a_{dg}(\lambda)$  in Eq. (15) are not independent in general, as an error in  $a(\lambda)$  may propagate to the retrieved  $a_{dg}(\lambda)$  (recall Fig. 4). We estimated the covariance  $\sigma_{xy}$  between  $a(\lambda)$  and  $a_{dg}(\lambda)$  from the synthetic dataset. Following Lee *et al.* [43], the uncertainty of total absorption coefficient at the reference wavelength 550 nm is empirically determined as

$$\Delta a(550) = 0.35[1 - 2.4e^{-16a(550)_{\text{est}}}]a(550)_{\text{est}}, \quad (16)$$

where  $a(550)_{\text{est}}$  is the QAA-retrieved total absorption. A constant value of 0.5 is assigned to the uncertainty of the exponent of particle backscattering spectra.

The QAA algorithm relies on two wavelengths of 410 and 440 nm; according to the synthesized data, the corresponding partition factor  $\zeta$  varies between 0.64 and 1.02 and  $\xi$  varies between 1.32 and 1.84. The QAA-UV algorithm makes use of 380 and 440 nm bands, for which  $\zeta$  changes from 0.06 to 0.98 and  $\xi$  varies in a range of 1.78–3.52. We assign values of  $\zeta$  and  $\xi$  to Eqs. (12)–(14) based on their respective statistics. First, the median values of  $\zeta$  and  $\xi$  are determined and hereby assigned to  $\zeta$  and  $\xi$ . Specifically, the QAA algorithm takes a constant of 0.84 for  $\zeta$  and 1.55 for  $\xi$ . For the QAA-UV algorithm, constant values of 0.46 and 2.43 were assigned to  $\zeta$  and  $\xi$ , respectively. According to Eq. (7), a  $\xi$  value equal to 1.55

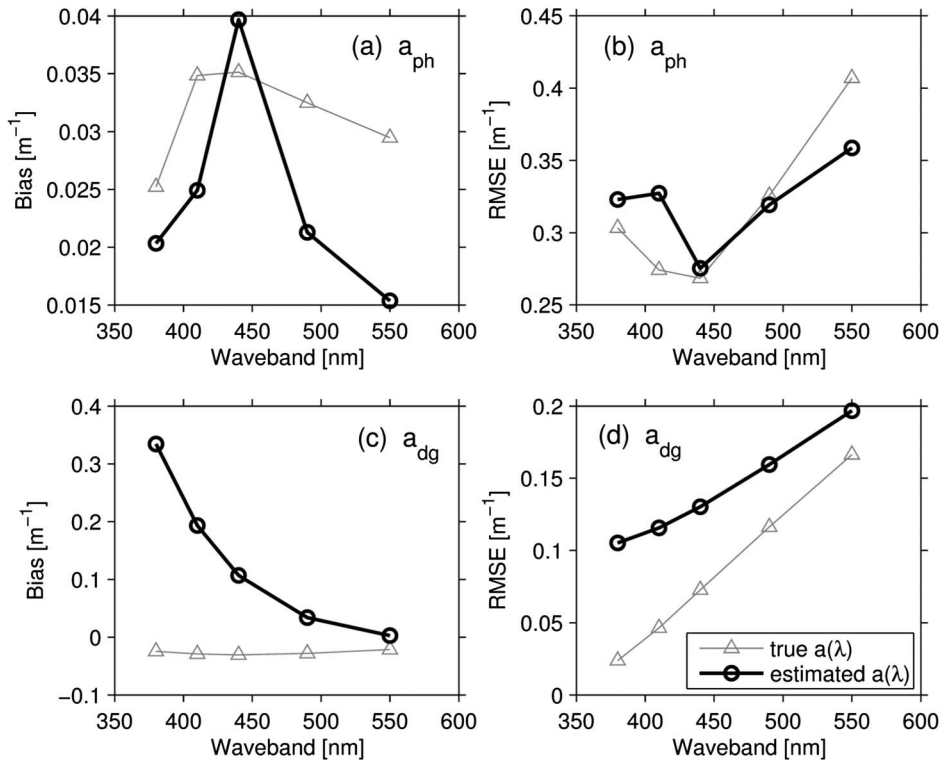


Fig. 4. Sensitivity of model retrievals to the total absorption coefficient  $a(\lambda)$ .

in the QAA model or 2.43 in the QAA-UV suggests  $S \approx 0.015 \text{ nm}^{-1}$ . The uncertainties in  $\Delta\zeta$  and  $\Delta\xi$  are determined as the range of variation from the medians. Specifically,  $\Delta\zeta = 0.15$  and  $\Delta\xi = 0.25$  are assigned to the QAA model; a value of  $\Delta\zeta = 0.15$  corresponds to a  $\zeta$  range of 0.68–0.98;  $\Delta\xi = 0.25$  indicates that  $\xi$  varies between 1.34 and 1.61 (equivalent  $S$  value is 0.010 to 0.016  $\text{nm}^{-1}$ ). For the QAA-UV model, values of 0.25 and 0.7 are assigned to  $\Delta\zeta$  and  $\Delta\xi$ , respectively. An uncertainty value  $\Delta\zeta = 0.25$  corresponds to a range of 0.20–0.7 for  $\zeta$ ;  $\Delta\xi = 0.7$  indicates that  $\xi$  varies between 1.87 and 3.37.

The obtained uncertainty in the model-derived  $a_{ph}(440)$  and  $a_{dg}(440)$  is illustrated in Fig. 5, where a Type II least square fit is applied to the log-transformed QAA-UV and QAA estimations. As shown in the plots, each data pair has a coefficient of determination  $R^2$  close to 1. To further quantify the relative difference between QAA-UV and QAA uncertainties, the symmetric absolute percentage difference (SMAPE) is calculated,  $\text{SMAPE} = 1/N \times \sum [2 \times (x_1^i - x_2^i) / (x_1^i + x_2^i)] \times 100\%$ . According to the SMAPE, the uncertainty associated with QAA-UV and QAA results at 440 nm is almost the same ( $\text{SMAPE} < 5\%$ ).

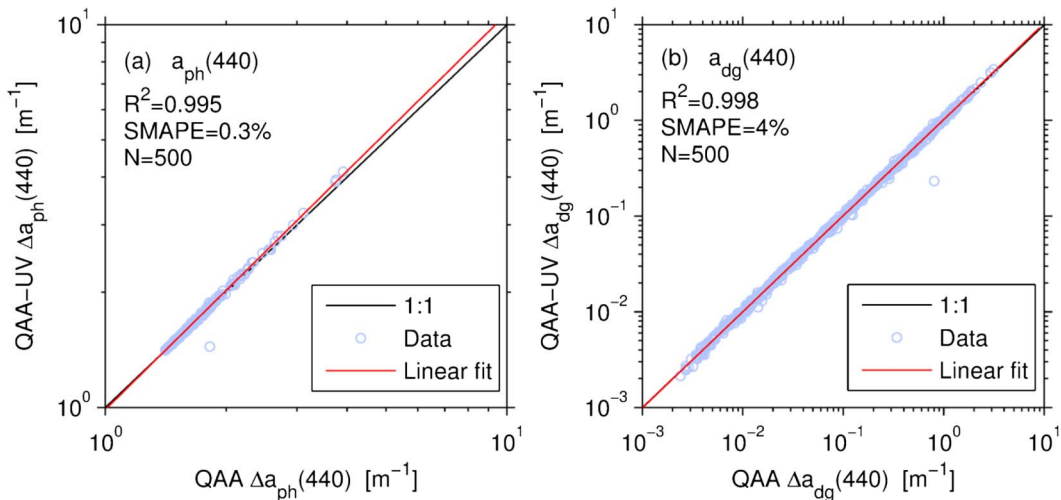


Fig. 5. Comparison of uncertainty in the model-derived component absorption  $a_{ph}(440)$  and  $a_{dg}(440)$ .

**Table 5. Comparison of the Algorithm Uncertainty of QAA-UV and QAA Model<sup>a</sup>**

		Spectral Band (units: nm)				
Parameter		380	410	440	490	550
$\Delta a_{ph}$	Mean $\pm$ Std <sup>b</sup>	1.98 $\pm$ 1.21 (1.96 $\pm$ 1.17)	1.68 $\pm$ 0.62 (1.68 $\pm$ 0.60)	1.54 $\pm$ 0.32 (1.54 $\pm$ 0.31)	1.45 $\pm$ 0.10 (1.45 $\pm$ 0.10)	1.42 $\pm$ 0.03 (1.42 $\pm$ 0.30)
	Slope	1.02	1.02	1.03	1.03	1.00
	Intercept	-0.01	-0.01	-0.01	-0.01	-0.00
	$R^2$	0.994	0.994	0.995	0.995	0.995
	SMAPE	1%	0.5%	0.3%	0.1%	0.03%
$\Delta a_{dg}$	Mean $\pm$ Std <sup>b</sup>	0.82 $\pm$ 1.30 (0.79 $\pm$ 1.24)	0.48 $\pm$ 0.77 (0.47 $\pm$ 0.74)	0.30 $\pm$ 0.48 (0.29 $\pm$ 0.46)	0.16 $\pm$ 0.25 (0.15 $\pm$ 0.24)	0.08 $\pm$ 0.13 (0.08 $\pm$ 0.13)
	Slope	1.02	1.02	1.02	1.02	1.02
	Intercept	0.03	0.02	0.02	0.03	0.06
	$R^2$	0.999	0.999	0.999	0.999	0.999
	SMAPE	5%	4%	4%	4%	4%

<sup>a</sup>A model II least square fit is applied to the log-transformed uncertainty.

<sup>b</sup>Mean uncertainty for QAA-UV retrievals and that of QAA retrievals (within the parentheses)

The uncertainty  $\Delta a_{ph}(\lambda)$  and  $\Delta a_{dg}(\lambda)$  are spectrally dependent, increasing toward the shorter wavelengths (Table 5). However, evidence from the Type II linear regression and the SMAPE errors all confirm that there is no significant difference in uncertainties between the QAA-UV model and the QAA model.

### C. Atmospheric Effects

The data quality of  $R_{rs}(\lambda)$  is critical for remote sensing retrievals, unless spectrally covarying errors in  $R_{rs}(\lambda)$  can be overcome with specially designed algorithms (e.g., [45]), whereas the  $R_{rs}(\lambda)$  discussed so far is model simulated (or “error free”). The  $R_{rs}(\lambda)$  spectra derived from the ocean color observation is subject to uncertainties due to imperfect atmospheric corrections [46,47], as well as sensor calibrations. It is not clear yet how the  $R_{rs}(\lambda)$  uncertainty ( $\Delta R_{rs}(\lambda)$ , unit:  $\text{sr}^{-1}$ ) impacts the performance of QAA-UV model on the retrievals of  $a_{ph}(\lambda)$  and  $a_{dg}(\lambda)$ . Hu *et al.* [48] have estimated the  $\Delta R_{rs}$  from the ocean color imagery in oceanic gyres and reported that  $\Delta R_{rs}(\lambda)$  is spectrally dependent, generally increasing toward shorter wavebands from the green bands in absolute sense. In the QAA system,

$\Delta R_{rs}(\lambda)$  will propagate to the total absorption coefficient and the two partition factors  $\zeta$  and  $\xi$  and further to the retrievals of  $a_{ph}(\lambda)$  and  $a_{dg}(\lambda)$ . To assess how  $\Delta R_{rs}(\lambda)$  impacts the model uncertainty of QAA-UV, we first estimated the mean absolute uncertainty  $\Delta R_{rs}(\lambda)$  by averaging the  $\Delta R_{rs}(\lambda)$  originally estimated from MODIS in the north Atlantic gyre for different chlorophyll a levels [48]. The spectral uncertainty was then linearly extrapolated to 380 nm band based on the information at wavebands 410, 440, 490, and 550 nm. The derived mean  $\Delta R_{rs}(\lambda)$  are 0.00084, 0.00063, 0.00042, 0.00038, 0.00023, and 0.000045  $\text{sr}^{-1}$ , in the wavelengths of 380, 410, 440, 490, 550, and 670 nm, respectively. The  $\Delta R_{rs}$  was then added to the simulated  $R_{rs}$  spectrum to generate an error-disturbed spectrum,  $R_{rs}^*$ , as the following:

$$R_{rs}^*(\lambda) = R_{rs}(\lambda) + \mathfrak{N} \cdot \Delta R_{rs}(\lambda), \quad (17)$$

where  $\mathfrak{N}$  is a random number of standard normal distribution. The absolute difference between the model derivations from inputs  $R_{rs}$  and  $R_{rs}^*$  was taken as the  $\Delta R_{rs}$ -induced uncertainty.

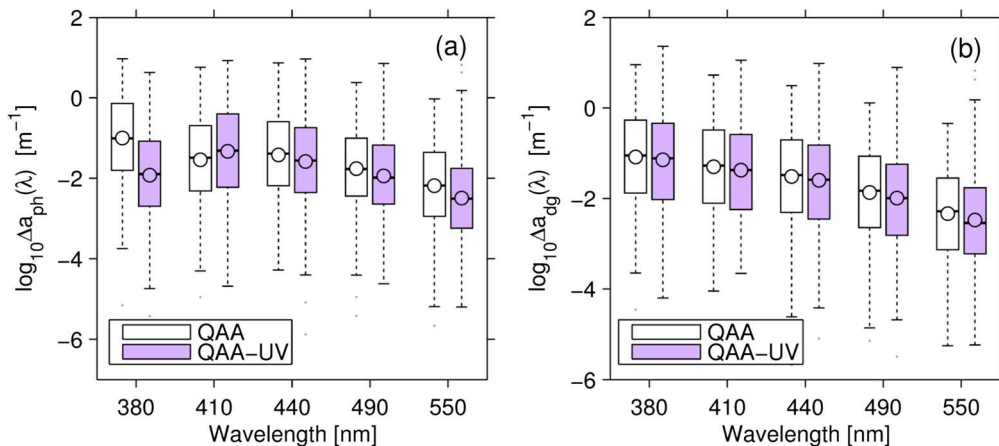


Fig. 6. Uncertainty in the model estimations induced by  $\Delta R_{rs}(\lambda)$ .

Figure 6 shows the spectral distribution of the resulted uncertainty in  $\Delta a_{ph}(\lambda)$  and  $\Delta a_{dg}(\lambda)$  with  $R_{rs}^*$ . Apparently both quantities are spectrally dependent. The  $\Delta a_{ph}(\lambda)$  has a minimum at waveband 550 nm [Fig. 6(a)]. Analogous to  $\Delta R_{rs}(\lambda)$ , the  $\Delta a_{ph}(\lambda)$  generally increases from the 550 nm band toward the 410 nm band. From 410 to 380 nm, it is noticeable that  $\Delta a_{ph}(\lambda)$  from QAA-UV is much smaller compared with that from QAA. The difference between the mean uncertainties at this band is significant according to the one-way ANOVA analysis ( $F(1, 870) = 127.8, p \approx 0$ ). The  $\Delta a_{dg}(\lambda)$  monotonically increases with decreasing wavelengths and has not shown significant difference between the two algorithms [Fig. 6(b)].

#### 4. Model Performance Evaluation with *In Situ* Data

##### A. Field Measurements

An *in situ* dataset with bio-optical properties and remote sensing reflectance is assembled to test the algorithm performance (Fig. 7). The primary dataset is formed through searching the SeaWiFS Bio-optical Archive and Storage System (SeaBASS) [49,50], which covers stations across the global oceans and was obtained during 2001–2011. The secondary dataset was obtained in the Southern Pacific Ocean during the Biogeochemistry and Optics South Pacific Experiment (BIOCOPE) campaign in 2004 [51].

The absorption coefficients of gelbstoff, detrital matter, and phytoplankton were measured with water samples collected with Niskin bottles following the protocols of [52–54]. Briefly, the sea water was filtered with 0.2  $\mu\text{m}$  filter, and then the filtrate is measured with the spectrometer for gelbstoff absorption. The seawater samples collected on the Whatman GF/F filters were measured with a spectrophotometer equipped for the total particulate absorption  $a_p(\lambda)$ . The absorption coefficients of detrital matters were then determined experimentally after extracting the pigments. The absorption coefficient of phytoplankton was eventually derived by subtracting  $a_d(\lambda)$  from  $a_p(\lambda)$ .

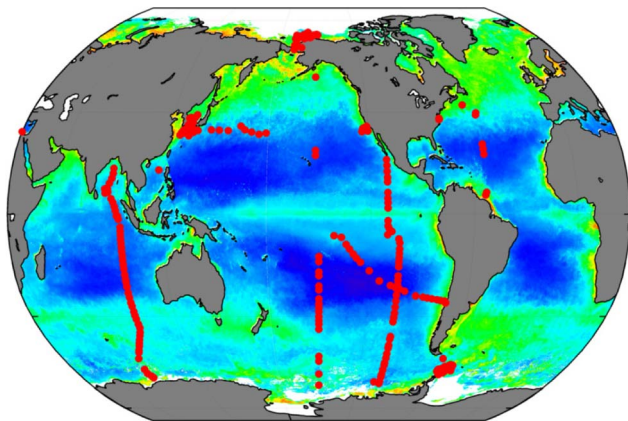


Fig. 7. Station map of *in situ* bio-optical measurements overlaid the SeaWiFS annual (year 2010) chlorophyll a map.

The radiometric data were collected using various instruments including the SeaWiFS profiling radiometer system (SPMR, Satlantic Inc), and the Biospherical MER series radiometers and the BioPRO profiling radiometer (Biospherical Instruments, Inc). The remote sensing reflectance was computed from the relationship,  $R_{rs}(\lambda) = 0.54L_u(0^-, \lambda)/E_s(\lambda)$ , where  $L_u(0^-)$  and  $E_s$  are the upwelling radiance right below the water surface and the downwelling plane irradiance just above the ocean, respectively, and both were derived from the radiometric measurements [55].

A quality control of the field data is carried out to remove negative values from subsequent analysis. We further set a threshold to the slope of the CDM spectral absorption as  $0.005 < S < 0.03 \text{ nm}^{-1}$ , which corresponds to absorption ratios of  $1.35 < a_{dg}(380)/a_{dg}(440) < 5.0$ . Those measurements beyond this domain are removed. The ranges of main optical parameters for the field data are compared with the synthetic data in Table 2. A further comparison of the distribution of the  $R_{rs}(\lambda)$  band ratios and absorption ratios of the *in situ* data and the synthetic data are given in Fig. 8. It is obvious that the *in situ* data points generally fall within the same domain of the synthetic data. This consistency supports the validity of the synthetic data presented in Section 2.A. Unlike the synthetic data, though, most of the *in situ* data are distributed in the blue ocean waters with  $R_{rs}(440)$  larger than  $R_{rs}(550)$  [Fig. 8(a)]. It is also noted that some of the extremely clear and oligotrophic oceanic waters with  $a_{ph}(440) < 0.005 \text{ m}^{-1}$  [56] are included in the *in situ* dataset but beyond the scope of the synthetic database. In total there are 209 stations valid for model evaluation.

##### B. Model Testing Results

Further quality control of the derived properties is implemented to remove the abnormal retrievals. As earlier model studies, for example, negative values are sometimes found with the model derived phytoplankton absorption coefficients, particularly for  $a_{ph}(380)$  and  $a_{ph}(550)$  from QAA and  $a_{ph}(550)$  from QAA-UV. Removal of such nonrealistic data reduced the number of valid retrievals, particularly for  $a_{ph}(380)$  and  $a_{ph}(550)$ .

The error statistics of the model estimations are summarized in Table 6. For the estimated  $a_{dg}(\lambda)$ , the QAA-UV algorithm has shown errors approximately equivalent to those of QAA. For the phytoplankton absorption estimation, however, QAA-UV actually resulted in a larger bias than QAA for most wavebands. There is one obvious exception at the UV band, where the RMSE (and nRMSE) error of the QAA-UV estimated  $a_{ph}(380)$  is much smaller (over  $0.2 \text{ m}^{-1}$ ) than that of the QAA estimation.

In comparison with the synthetic data in Table 4, the  $a_{ph}$  and  $a_{dg}$  derived from the measured remote sensing reflectance is much noisier. The (absolute) magnitudes of the errors presented in Table 6 are

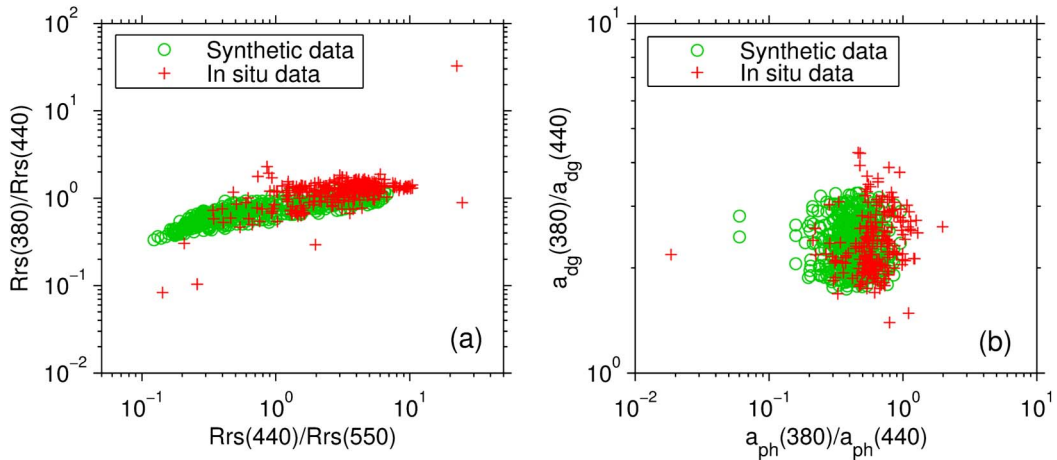


Fig. 8. Comparison of synthesized and measured bio-optical data. (a) Ranges and variations of  $R_{rs}(380)/R_{rs}(440)$  and  $R_{rs}(440)/R_{rs}(550)$ . (b) Ranges and variations of  $a_{dg}(380)/a_{dg}(440)$  and  $a_{ph}(380)/a_{ph}(440)$ .

Table 6. Error Statistics between the Model-Estimated Absorption Coefficient and Field Measured Absorption Coefficient<sup>a</sup>

	Band (nm)	$N$	$n$	$R^2$	RMSE (m <sup>-1</sup> )	nRMSE (%)	Bias (m <sup>-1</sup> )
$a_{ph}(\lambda)$	380	80(80)	80(80)	0.16(0.29)	<b>0.53(0.74)</b>	<b>30.0(40.1)</b>	-0.03(-0.02)
	410	199(199)	199(199)	0.17(0.56)	0.50(0.33)	26.3(17.5)	<b>-0.006(-0.008)</b>
	440	200(200)	200(200)	0.40(0.55)	0.37(0.31)	20.5(17.5)	-0.009(-0.007)
	490	199(199)	199(199)	0.44(0.51)	0.43(0.37)	21.7(18.8)	-0.009(-0.004)
	550	101(101)	101(101)	0.42(0.43)	0.75(0.75)	30.2(30.0)	-0.006(0.001)
$a_{dg}(\lambda)$	380	206(206)	206(206)	0.55(0.54)	0.43(0.33)	35.2(26.8)	-0.09(-0.08)
	410	199(199)	199(199)	0.55(0.53)	0.43(0.35)	31.1(25.1)	-0.04(-0.03)
	440	207(207)	207(207)	0.54(0.52)	0.41(0.35)	25.9(22.3)	-0.02(-0.02)
	490	207(207)	207(207)	0.48(0.47)	0.41(0.40)	21.4(20.5)	-0.009(-0.009)
	550	187(187)	187(187)	0.44(0.46)	0.40(0.39)	17.4(17.2)	<b>-0.003(-0.004)</b>

<sup>a</sup>The QAA derivations are presented within parentheses.  $N$  is the total number of observations and  $n$  is the number of valid observations. The bold values indicate that the accuracy of model estimations has been improved by QAA-UV algorithm.

much greater than the estimations based on the synthetic data in Table 4. The phenomena can be partly ascribed to the fact that the field measurements of  $R_{rs}$  and the measured inherent optical properties used for comparison are not error free. Although the exact measurement errors are unknown, it is certain that these errors will add to the retrievals of  $a_{ph}(\lambda)$  and  $a_{dg}(\lambda)$ . Further, the absorption coefficient of pure seawater in the shorter wavelengths is still questionable [37,38], which will also contribute to errors in the retrieved  $a_{ph}(\lambda)$  and  $a_{dg}(\lambda)$  from QAA or QAA-UV.

## 5. Discussion

The CDM absorption  $a_{dg}$  increases exponentially with the decrease of wavelength while the phytoplankton absorption  $a_{ph}$  decreases with the decrease of wavelength from about 440 nm (see Fig. 1). The  $a_{ph}$  spectral ratio ( $\zeta$ ) of the QAA-UV pair (380 and 440 nm) is almost always smaller than that of the QAA pair (410 and 440 nm), while the  $a_{dg}$  spectral ratio ( $\xi$ ) for the QAA-UV pair is significantly larger than that of the QAA (Fig. 9). Because of the enhanced spectral contrast between  $a_{ph}$  and  $a_{dg}$  in the shorter wavelengths, the improvement in the retrievals of  $a_{ph}(\lambda)$  and  $a_{dg}(\lambda)$  with remote

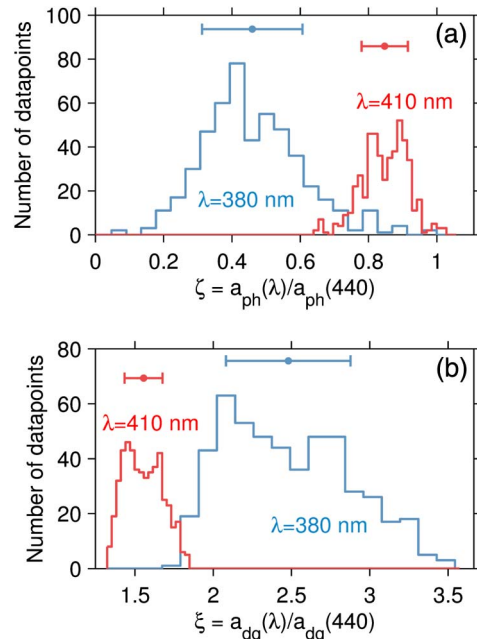


Fig. 9. Histograms of absorption ratios at two primary wavebands: (a) phytoplankton absorption ratio and (b) CDM absorption ratio. The mean value and standard deviation are overlaid for each quantity.

sensing reflectance at an UV band is anticipated provided that  $a(\lambda)$  can be accurately estimated (Table 4).

The improvement of QAA-UV on the separation of  $a_{ph}(\lambda)$  and  $a_{dg}(\lambda)$  is, however, not obvious when the algorithms are applied to data from field measurements (Table 6). In particular, it is noticeable that the results in Table 6 are not as good as those shown in [19,20,22]. In the mid-Atlantic Bight, for example, the  $a_{dg}(440)$  was estimated from the  $R_{rs}$  band ratio,  $a_{dg}(440) = \ln((R_{rs}(490)/R_{rs}(550) - 0.436)/2.221 - 13.126)$ , with RMSE of  $\sim 0.14$  [22]. There are a couple of reasons responsible for this discrepancy. First and foremost, QAA and QAA-UV (which switches out the 410 nm band with 380 nm) are mechanistic algorithms based on relationships developed from the radiative transfer equation, which fundamentally requires a closure between the measured  $R_{rs}$  and IOPs. The algorithms in [19,20,22], on the other hand, are empirical in nature, directly relating the CDM absorption to band ratios of remote sensing reflectance and thus bypassing the requirement of closure between  $R_{rs}$  and IOPs. Second, presently QAA and QAA-UV (as well as other semi-analytical algorithms) predetermine a spectral slope  $S$  for  $a_{dg}(\lambda)$  for the separation of  $a_{ph}(\lambda)$  and  $a_{dg}(\lambda)$ , a process not required in the empirical algorithms, and error in this determination could significantly affect the retrieval of  $a_{ph}(\lambda)$  and/or  $a_{dg}(\lambda)$  (recall Fig. 3). Future analytical algorithms should focus on improving the determination of  $S$  from  $R_{rs}(\lambda)$  to fully take advantage of the ocean color measurements in the UV bands. And third, the retrieval of  $a_{ph}(\lambda)$  and  $a_{dg}(\lambda)$  in both QAA and QAA-UV uses the total absorption coefficient  $a(\lambda)$  derived from  $R_{rs}(\lambda)$ , and any error associated with  $a(\lambda)$  will likely propagate to either  $a_{ph}(\lambda)$  or  $a_{dg}(\lambda)$  or both [57]. Thus further improvement of the estimation of  $a(\lambda)$  is necessary. Furthermore, the uncertainties of QAA-UV derived  $a_{ph}(\lambda)$  and  $a_{dg}(\lambda)$  include uncertainties from the measured  $R_{rs}$ , which is different from empirical fittings between  $a_{dg}(\lambda)$  and  $R_{rs}$ , where any error in  $R_{rs}$  will be transferred to the empirical coefficients. The radiance at the top of atmosphere (TOA) is mostly contributed by the atmospheric signals. In the UV domain, only about 5% of the water-leaving radiance can reach the TOA. The current atmospheric correction scheme is performed by extrapolating the aerosol optical properties from the NIR band [58] or SWIR bands [59]. Small errors made at these bands will propagate to and become significant at the UV band. As a result, because of likely higher  $R_{rs}$  uncertainty in the UV band due to imperfect atmospheric correction [48], larger uncertainty in QAA-UV derived  $a_{dg}(380)$  is expected when it is applied to satellite measurements. This situation can become much severer in turbid coastal waters, where the UV water-leaving radiance signal may reach negligible levels (e.g., He *et al.* [60]). Therefore, to analytically apply ocean color measurements in the UV band for the retrieval of water constituents,

as for the visible bands, it is critical to have reliable atmospheric correction.

## 6. Conclusions

We modified the QAA by replacing the 410 nm band with 380 nm band (QAA-UV) for analytical retrieval of phytoplankton and CDM absorption coefficients from the remote sensing reflectance spectrum. Applying QAA-UV to a synthetic dataset has demonstrated that the retrievals of  $a_{ph}(\lambda)$  and  $a_{dg}(\lambda)$  are improved relative to the standard QAA. The finding has confirmed the long-standing presumption on the application of UV-band ocean color observations in improving the separation of phytoplankton and CDM. On the other hand, the improvement is not uniform between  $a_{ph}(\lambda)$  and  $a_{dg}(\lambda)$  and not obvious for measurements made *in situ*. In addition, because of the analytical and two-step nature of QAA or QAA-UV algorithms, it is important to obtain accurate retrieval of  $a(\lambda)$  for the decomposition of  $a_{ph}(\lambda)$  and  $a_{dg}(\lambda)$ , whereas the accuracy of  $a(\lambda)$  is directly related to the accuracy of  $R_{rs}(\lambda)$ , which further depends on the performance of atmosphere correction for ocean color satellite remote sensing. Because  $R_{rs}(\lambda)$  in the UV domain makes very small contributions to radiance measurements at the satellite altitude, it poses a daunting challenge to the community to obtain reliable water-leaving radiance in the UV band for analytically retrieval of water constituents, in particular for CDM rich coastal and inland waters.

This study benefits from the SeaBASS data archive system, and we thank those researchers who contributed their data to this database. The authors are also grateful to the French researchers who have generously shared with us the field measurements during the BIOSOPE project. This study was funded by the National Aeronautic and Space Administration (NASA) Ocean Biology and Biogeochemistry and Water and Energy Cycle Programs, and the National Oceanic and Atmospheric Administration (NOAA) JPSS VIIRS Ocean Color Cal/Val Project. We thank two anonymous reviewers for the comments and suggestions.

## References

1. C. B. Field, M. J. Behrenfeld, J. T. Randerson, and P. G. Falkowski, "Primary production of the biosphere: integrating terrestrial and oceanic components," *Science* **281**, 237–240 (1998).
2. J. T. O. Kirk, *Light and Photosynthesis in Aquatic Ecosystems*, 2nd ed. (Cambridge University, 1994), p. 509.
3. D. A. Siegel, S. Maritorena, N. B. Nelson, M. J. Behrenfeld, and C. R. McClain, "Colored dissolved organic matter and its influence on the satellite-based characterization of the ocean biosphere," *Geophys. Res. Lett.* **32**, L20605 (2005).
4. M. J. Behrenfeld, E. Boss, D. Siegel, and D. M. Shea, "Carbon-based ocean productivity and phytoplankton physiology from space," *Global Biogeochem Cycles* **19**, GB1006 (2005).
5. C. R. McClain, "A decade of satellite ocean color observations," *Ann. Rev. Mar. Sci.* **1**, 19–42 (2009).
6. Z. P. Lee, K. L. Carder, and R. Arnone, "Deriving inherent optical properties from water color: a multi-band quasi-analytical algorithm for optically deep waters," *Appl. Opt.* **41**, 5755–5772 (2002).

7. S. Maritorena, D. A. Siegel, and A. R. Peterson, "Optimization of a semianalytical ocean color model for global-scale applications," *Appl. Opt.* **41**, 2705–2714 (2002).
8. F. E. Hoge and P. E. Lyon, "Satellite retrieval of inherent optical properties by linear matrix inversion of oceanic radiance models: an analysis of model and radiance measurement errors," *J. Geophys. Res.* **101**, 16631–16648 (1996).
9. S. Shang, Q. Dong, Z. Lee, Y. Li, Y. Xie, and M. Behrenfeld, "MODIS observed phytoplankton dynamics in the Taiwan Strait: an absorption-based analysis," *Biogeosciences* **8**, 841–850 (2011).
10. Z. P. Lee, S. Shang, C. Hu, M. Lewis, R. Arnone, Y. Li, and B. Lubac, "Time series of bio-optical properties in a subtropical gyre: implications for the evaluation of inter-annual trends of biogeochemical properties," *J. Geophys. Res.* **115**, C09012 (2010).
11. D. A. Siegel, M. J. Behrenfeld, S. Maritorena, C. R. McClain, D. Antoine, S. W. Bailey, P. S. Bontempi, E. S. Boss, H. M. Dierssen, S. C. Doney, R. E. Eplee, Jr., R. H. Evans, G. C. Feldman, E. Fields, B. A. Franz, N. A. Kuring, C. Mengelt, N. B. Nelson, F. S. Patt, W. D. Robinson, J. L. Sarmiento, C. M. Swan, P. J. Werdell, T. K. Westberry, J. G. Wilding, and J. A. Yoder, "Regional to global assessments of phytoplankton dynamics from the SeaWiFS mission," *Remote Sens. Environ.* **135**, 77–91 (2013).
12. Z. P. Lee, V. P. Lance, S. Shang, R. Vaillancourt, S. Freeman, B. Lubac, B. R. Hargreaves, C. Del Castillo, R. Miller, M. Twardowski, and G. Wei, "An assessment of optical properties and primary production derived from remote sensing in the Southern Ocean (SO GasEx)," *J. Geophys. Res.* **116**, C00F03 (2011).
13. J. E. O'Reilly, S. Maritorena, M. C. O'Brien, D. A. Siegel, D. A. Toole, D. W. Menzies, R. C. Smith, J. L. Mueller, B. G. Mitchell, M. Kahru, F. P. Chavez, P. Strutton, G. F. Cota, S. B. Hooker, C. R. McClain, K. L. Carder, F. E. Muller-Karger, L. W. Harding, A. Magnuson, D. A. Phinney, G. F. Moore, J. Aiken, K. R. Arrigo, R. M. Letelier, and M. Culver, "SeaWiFS postlaunch calibration and validation analyses, Part 3," in *SeaWiFS Postlaunch Technical Report Series*, S. B. Hooker and E. R. Firestone, eds. (NASA Goddard Space Flight Center, 2000), p. 58.
14. A. Morel and H. R. Gordon, "Report of the working group on water color," *Bound.-Lay. Meteorol.* **18**, 343–355 (1980).
15. K. L. Carder, S. K. Hawes, K. A. Baker, R. C. Smith, R. G. Steward, and B. G. Mitchell, "Reflectance model for quantifying chlorophyll *a* in the presence of productivity degradation products," *J. Geophys. Res.* **96**, 20599–20611 (1991).
16. S. Sathyendranath, L. Prieur, and A. Morel, "A three-component model of ocean colour and its application to remote sensing of phytoplankton pigments in coastal waters," *Int. J. Remote Sens.* **10**, 1373–1394 (1989).
17. A. Morel and B. Gentili, "A simple band ratio technique to quantify the colored dissolved and detrital organic material from ocean color remotely sensed data," *Remote Sens. Environ.* **113**, 998–1011 (2009).
18. Z. P. Lee, K. L. Carder, R. G. Steward, T. G. Peacock, C. O. Davis, and J. S. Path, "An empirical algorithm for light absorption by ocean water based on color," *J. Geophys. Res.* **103**, 27967–27978 (1998).
19. B. G. Mitchell and M. Kahru, "Bio-optical algorithms for ADEOS-2 GLI," *J. Remote Sens. Soc. Japan* **29**, 80–85 (2009).
20. M. Tedetti, B. Charrière, A. Bricaud, J. Para, P. Raimbault, and R. Sempéré, "Distribution of normalized water-leaving radiances at UV and visible wave bands in relation with chlorophyll *a* and colored detrital matter content in the south-east Pacific," *J. Geophys. Res.* **115**, C02010 (2010).
21. A. Mannino, M. G. Novak, S. B. Hooker, K. Hyde, and D. Aurin, "Algorithm development and validation of CDOM properties for estuarine and continental shelf waters along the northeastern U.S. coast," *Remote Sens. Environ.* **152**, 576–602 (2014).
22. A. Mannino, M. E. Russ, and S. B. Hooker, "Algorithm development and validation for satellite-derived distributions of DOC and CDOM in the US Middle Atlantic Bight," *J. Geophys. Res.* **113**, C07051 (2008).
23. A. Bricaud, A. Morel, and L. Prieur, "Absorption by dissolved organic matter of the sea (yellow substance) in the UV and visible domains," *Limnol. Oceanogr.* **26**, 43–53 (1981).
24. C. E. Del Castillo, "Remote sensing of organic matter in coastal waters," in *Remote Sensing of Coastal Aquatic Environments: Technologies, Techniques and Applications*, R. L. Miller, C. E. Del Castillo, and B. A. McKee, eds. (Springer, 2005), pp. 157–180.
25. H. M. Dierssen, "Perspectives on empirical approaches for ocean color remote sensing of chlorophyll in a changing climate," *Proc. Natl. Acad. Sci. USA* **107**, 17073–17078 (2010).
26. W. W. Gregg and N. W. Casey, "Global and regional evaluation of the SeaWiFS chlorophyll data set," *Remote Sens. Environ.* **93**, 463–479 (2004).
27. T. S. Moore, J. W. Campbell, and M. D. Dowell, "A class-based approach to characterizing and mapping the uncertainty of the MODIS ocean chlorophyll product," *Remote Sens. Environ.* **113**, 2424–2430 (2009).
28. M. Szeto, P. J. Werdell, T. S. Moore, and J. W. Campbell, "Are the world's oceans optically different?" *J. Geophys. Res.* **116**, C00H04 (2011).
29. C. A. Brown, Y. Huot, P. J. Werdell, B. Gentili, and H. Claustre, "The origin and global distribution of second order variability in satellite ocean color and its potential applications to algorithm development," *Remote Sens. Environ.* **112**, 4186–4203 (2008).
30. C. Del Castillo, S. Platnick, D. Antoine, B. Balch, M. Behrenfeld, E. S. Boss, B. Cairns, J. Chowdhary, A. DaSilva, D. Diner, O. Dubovik, B. Franz, R. Frouin, W. Gregg, K. F. Huemmrich, R. Kahn, A. Marshak, S. Massie, C. McClain, C. McNaughton, G. Meister, G. Mitchell, F. Muller-Karger, J. Puschell, J. Riedi, D. Siegel, M. Wang, and J. Werdell, "Pre-Aerosol, Clouds, and Ocean Ecosystem (PACE) Mission," Science Definition Team Report (NASA, 2012), p. 274.
31. M. Wang, "Remote sensing of the ocean contributions from ultraviolet to near-infrared using the shortwave infrared bands: simulations," *Appl. Opt.* **46**, 1535–1547 (2007).
32. Z.-P. Lee, ed. "Remote Sensing of Inherent Optical Properties: Fundamentals, Tests of Algorithms, and Applications," Reports of the International Ocean Color Coordinating Group No. 5 (IOCCG, 2006), p. 126.
33. Z. P. Lee, K. Carder, R. Arnone, and M. He, "Determination of primary spectral bands for remote sensing of aquatic environments," *Sensors* **7**, 3428–3441 (2007).
34. N. Hoepffner and S. Sathyendranath, "Determination of the major groups of phytoplankton pigments from the absorption spectra of total particulate matter," *J. Geophys. Res.* **98**, 22789–22803 (1993).
35. K. L. Carder, F. R. Chen, Z. P. Lee, S. K. Hawes, and D. Kamykowski, "Semianalytic moderate-resolution imaging spectrometer algorithms for chlorophyll-*a* and absorption with bio-optical domains based on nitrate-depletion temperatures," *J. Geophys. Res.* **104**, 5403–5421 (1999).
36. C. S. Roesler, M. J. Perry, and K. L. Carder, "Modeling *in situ* phytoplankton absorption from total absorption spectra in productive inland marine waters," *Limnol. Oceanogr.* **34**, 1510–1523 (1989).
37. R. M. Pope and E. S. Fry, "Absorption spectrum (380–700 nm) of pure water. II. Integrating cavity measurements," *Appl. Opt.* **36**, 8710–8723 (1997).
38. A. Morel, "Optical properties of pure water and pure sea water," in *Optical Aspects of Oceanography*, N. G. Jerlov and E. Steemann Nielsen, eds. (Academic, 1974), p. 494.
39. Z. P. Lee, K. L. Carder, and K. P. Du, "Effects of molecular and particle scatterings on model parameters for remote-sensing reflectance," *Appl. Opt.* **43**, 4957–4964 (2004).
40. H. R. Gordon, O. B. Brown, R. H. Evans, J. W. Brown, R. C. Smith, K. S. Baker, and D. K. Clark, "A semianalytic radiance model of ocean color," *J. Geophys. Res.* **93**, 10909–10924 (1988).
41. Z. P. Lee, K. L. Carder, C. D. Mobley, R. G. Steward, and J. S. Patch, "Hyperspectral remote sensing for shallow waters: 2. Deriving bottom depths and water properties by optimization," *Appl. Opt.* **38**, 3831–3843 (1999).

42. Z. P. Lee, B. Lubac, J. Werdell, and R. Arnone, "An update of the quasi-analytical algorithm (QAA\_v5)," (2009), retrieved [http://www.ioceg.org/groups/Software\\_OCA/QAA\\_v5.pdf](http://www.ioceg.org/groups/Software_OCA/QAA_v5.pdf).
43. Z. P. Lee, R. Arnone, C. Hu, P. J. Werdell, and B. Lubac, "Uncertainties of optical parameters and their propagations in an analytical ocean color inversion algorithm," *Appl. Opt.* **49**, 369–381 (2010).
44. C. E. Del Castillo and R. L. Miller, "Horizontal and vertical distributions of colored dissolved organic matter during the Southern Ocean Gas Exchange Experiment," *J. Geophys. Res.* **116**, C00F07 (2011).
45. C. Hu, Z. P. Lee, and B. Franz, "Chlorophyll a algorithms for oligotrophic oceans: a novel approach based on three-band reflectance difference," *J. Geophys. Res.* **117**, C01011 (2012).
46. H. R. Gordon, "Atmospheric correction of ocean color imagery in the Earth observing system era," *J. Geophys. Res.* **102**, 17081–17106 (1997).
47. D. Antoine, F. d'Ortenzio, S. B. Hooker, G. Bécu, B. Gentili, D. Tailliez, and A. J. Scott, "Assessment of uncertainty in the ocean reflectance determined by three satellite ocean color sensors (MERIS, SeaWiFS and MODIS-A) at an offshore site in the Mediterranean Sea (BOUSSOLE project)," *J. Geophys. Res.* **113**, C07013 (2008).
48. C. Hu, L. Feng, and Z. P. Lee, "Uncertainties of SeaWiFS and MODIS remote sensing reflectance: implications from clear water measurements," *Remote Sens. Environ.* **133**, 168–182 (2013).
49. P. J. Werdell, S. Bailey, G. Fargion, C. Pietras, K. Knobelspiesse, G. Feldman, and C. McClain, "Unique data repository facilitates ocean color satellite validation," *EoS Trans. Amer. Geophys. Union* **84**, 377–387 (2003).
50. S. B. Hooker, C. R. McClain, J. K. Firestone, T. L. Westphal, E.-N. Yeh, and Y. Ge, "*The SeaWiFS bio-optical archive and storage system (SeaBASS), Part 1*," (NASA Goddard Space Flight Center, 1994).
51. H. Claustre, A. Sciandra, and D. Vaultot, "Introduction to the special section bio-optical and biogeochemical conditions in the South East Pacific in late 2004: the BIOSOPE program," *Biogeosciences* **5**, 679–691 (2008).
52. A. Bricaud, M. Babin, H. Claustre, J. Ras, and F. Tieche, "Light absorption properties and absorption budget of South-east Pacific waters," *J. Geophys. Res.* **115**, C08009 (2010).
53. N. B. Nelson, D. A. Siegel, C. A. Carlson, C. Swan, W. M. Smethie, Jr., and S. Khatiwala, "Hydrography of chromophoric dissolved organic matter in the North Atlantic," *Deep-Sea Research, Part I* **54**, 710–731 (2007).
54. B. G. Mitchell, A. Bricaud, K. L. Carder, J. Cleveland, G. Ferrari, R. Gould, M. Kahru, M. Kishino, H. Maske, T. Moisan, L. Moore, N. Nelson, D. Phinney, R. Reynolds, H. Sosik, D. Stramski, S. Tassan, C. Trees, A. Weidemann, J. Weiland, and A. Vodacek, "Determination of spectral absorption coefficients of particles, dissolved material, and phytoplankton for discrete water samples" in *Ocean Optics Protocols for Satellite Ocean Color Sensor Validation, NASA/TM-2000-209966* (Goddard Space Flight Center, NASA, 2000).
55. J. L. Mueller, G. S. Fargion, and C. R. McClain, eds., *Ocean Optics Protocols for Satellite Ocean Color Sensor Validation, Revision 4, NASA/TM-2003-21621/Rev-Vol III* (NASA, Goddard Space Flight Center, 2003), Vol. **III**, p. 78.
56. A. Morel and B. Gentili, "The most oligotrophic subtropical zones of the global oceans: similarities and differences in terms of chlorophyll and yellow substance," *Biogeosciences* **7**, 3139–3151 (2010).
57. G. Zheng, D. Stramski, and R. A. Reynolds, "Evaluation of the Quasi-Analytical Algorithm for estimating the inherent optical properties of seawater from ocean color: comparison of Arctic and lower-latitude waters," *Remote Sens. Environ.* **155**, 194–209 (2014).
58. M. Wang, ed., "Atmospheric Correction for Remotely Sensed Ocean Color Products," *Reports of the International Ocean-Colour Coordinating Group, No. 10* (IOCCG, 2010), p. 78.
59. M. Wang and W. Shi, "The NIR-SWIR combined atmospheric correction approach for MODIS ocean color data processing," *Opt. Express* **15**, 15722–15733 (2007).
60. X. He, Y. Bai, D. Pan, J. Tang, and D. Wang, "Atmospheric correction of satellite ocean color imagery using the ultraviolet wavelength for highly turbid waters," *Opt. Express* **20**, 20754–20770 (2012).